

Braiding Lateral Morphotropic Grain Boundaries in Homogenetic Oxides

Shengru Chen, Qinghua Zhang, Dongke Rong, Yue Xu, Jinfeng Zhang, Fangfang Pei, He Bai, Yan-Xing Shang, Shan Lin, Qiao Jin, Haitao Hong, Can Wang, Wensheng Yan, Haizhong Guo, Tao Zhu, Lin Gu, Yu Gong, Qian Li, Lingfei Wang, Gang-Qin Liu, Kui-juan Jin,* and Er-Jia Guo*

Interfaces formed by correlated oxides offer a critical avenue for discovering emergent phenomena and quantum states. However, the fabrication of oxide interfaces with variable crystallographic orientations and strain states integrated along a film plane is extremely challenging by conventional layer-by-layer stacking or self-assembling. Here, the creation of morphotropic grain boundaries (GBs) in laterally interconnected cobaltite homostructures is reported. Single-crystalline substrates and suspended ultrathin freestanding membranes provide independent templates for coherent epitaxy and constraint on the growth orientation, resulting in seamless and atomically sharp GBs. Electronic states and magnetic behavior in hybrid structures are laterally modulated and isolated by GBs, enabling artificially engineered functionalities in the planar matrix. This work offers a simple and scalable method for fabricating unprecedented innovative interfaces through controlled synthesis routes as well as providing a platform for exploring potential applications in neuromorphics, solid-state batteries, and catalysis.

1. Introduction

Advanced thin-film deposition techniques enable scientists to fabricate high-quality oxide interfaces exhibiting emergent phenomena not found in bulk constituents.^[1–3] Interfaces naturally break spatial inversion symmetry, resulting in the reconstruction of electronic degrees of freedom at the nanoscale.^[4,5] These features typically improve the effects of electron correlations such as the reduction of bandwidths and dispersion, changes in crystal fields and shifts of Madelung energies,^[6] significantly impacting macroscopic physical properties. Therefore, interfaces have several intriguing and potentially useful effects, including high-temperature ferromagnetism, high- T_C superconductivity, electronic phase transitions

S. Chen, Q. Zhang, D. Rong, Y. Xu, Y.-X. Shang, S. Lin, Q. Jin, H. Hong, C. Wang, T. Zhu, G.-Q. Liu, K.-j. Jin, E.-j. Guo
Beijing National Laboratory for Condensed Matter Physics and Institute of Physics
Chinese Academy of Sciences
Beijing 100190, China
E-mail: kjjin@iphy.ac.cn; ejguo@iphy.ac.cn

S. Chen, Q. Jin, H. Hong, C. Wang, T. Zhu, G.-Q. Liu, K.-j. Jin, E.-j. Guo
Department of Physics & Center of Materials Science and Optoelectronics Engineering
University of Chinese Academy of Sciences
Beijing 100049, China

J. Zhang, L. Wang
Hefei National Laboratory for Physical Science at the Microscale
University of Science and Technology of China
Hefei 230026, China

F. Pei, W. Yan, Q. Li
National Synchrotron Radiation Laboratory
University of Science and Technology of China
Hefei 230029, China

H. Bai, T. Zhu
Spallation Neutron Source Science Center
Dongguan 523803, China

C. Wang, T. Zhu, G.-Q. Liu, K.-j. Jin, E.-j. Guo
Songshan Lake Materials Laboratory
Dongguan, Guangdong 523808, China

H. Guo
Key Laboratory of Material Physics & School of Physics and Microelectronics
Zhengzhou University
Zhengzhou 450001, China

L. Gu
National Center for Electron Microscopy in Beijing and School of Materials Science and Engineering
Tsinghua University
Beijing 100084, China

Y. Gong
Department of Physics and Astronomy
College of Charleston
58 Coming Street, Charleston, SC 29424, USA

 The ORCID identification number(s) for the author(s) of this article can be found under <https://doi.org/10.1002/adma.202206961>.

DOI: 10.1002/adma.202206961

and multiferroicity.^[7–10] Although a broad range of oxide interfaces have been synthesized and maturely investigated over decades, the conventional epitaxy focuses primarily on functional multilayers and superlattices stacked vertically layer-by-layer.^[11–13] High-quality epitaxial growth occurs only between dissimilar materials with similar crystal structures and close lattice constants. Beyond certain thresholds, an increasing number of defects and dislocations will form at interfaces, severely degrading their functionalities. In such cases, underlying substrates determine the crystallographic orientation, symmetry, and misfit strain of epitaxial layers grown on the surface. Another type of interface is aligned vertically in self-assembled arrayed nanostructures.^[14] Intrinsic similarities in the crystal chemistry, for example, oxygen coordination and electronegativity, allow the tantalizing possibility of epitaxy in three dimensions. Nanoscale clusters of ferro-/ferrimagnetic materials embedded in a ferroelectric matrix exhibit strong mechanical coupling between two ferroic order parameters, piquing a growing interest in developing multiferroic devices based on composite heterostructures.^[15] Success in these endeavors unquestionably promote the comprehensive understanding of correlated electron materials as well as their incorporation into practical applications.

Developing feasible strategies for fabricating innovative oxide interfaces provides many opportunities in both fundamental research and evolutionary devices. Lateral homostructures exhibit in-plane spatial modulations of the structural and physical properties of an identical single crystal in contrast to well-defined longitudinal heterostructures. One famous example is the formation of a morphotropic phase boundary in bismuth ferrite (BiFeO₃) films through an epitaxial constraint.^[16] Both tetragonal- and rhombohedral-like phases coexist within a single film and can be reversibly switched by an electric field and mechanical force.^[16,17] The boundary between two distinct phases significantly modulates surface morphology and exhibits an enhanced domain wall conductance in topologically confined nanoislands, implying great potential in non-volatile memory and actuator applications.^[18] In-plane spatially patterned electronic textures can also be achieved in ferromagnetic manganite and cobaltite single films by combining surface miscut steps and domain patterns via striped strain modulation.^[19,20] Furthermore, modification to the lattice symmetry in the film plane has been established in oxide films through low energy helium implantation post growth.^[21,22] This non-destructive strain doping approach is readily applied locally down to the micrometer scale to the same sample, effectively altering the crystal's total anisotropy energy and magnetic properties. From the traditional thin-film epitaxy perspective, the growth of lateral phase boundaries in homostructures composed of various crystallographic orientations and in-plane strain states remains a significant challenge. To remove the constraint regularity from single crystal substrates, a strategy that bypasses these restrictions in thin-film epitaxy is highly required. We noticed that a recent work by Wu et al. reported the growth of twisted multiferroic oxide lateral homostructures using freestanding membranes.^[23] The functional oxide layers can be rotated and stacked with designed twisting angles, adding another degree of freedom to design thin film properties. However, the fabrication method involves the hydrochloric acid as etching materials.

The unavoidable chemical residual and relatively large surface roughness of transferred membranes result in a great challenge in fabricating atomic-thin spatial gap between membrane and substrate. These factors inevitably influence the flatness, crystallinity and adhesiveness of subsequent grown layers, as well as the sharpness of morphotropic grain boundaries (GBs). Recent progresses in the synthesis of atomically thin membranes using water-soluble sacrificial layers allow us to develop ultrathin freestanding membranes with ultrasharp interfaces without using highly corrosive acid.

Here, we applied chemical free and environmentally friendly strategy in which only the deionized water is required to synthesize ≈8-unit-cell thick freestanding single crystal membranes. These high-quality membranes attached firmly onto the substrates maintain a minimum spatial gap down to ≈1 nm without forming chemical bonds, allowing these membranes to maintain their original structural geometries. Ferromagnetic oxide films epitaxially grown on both membranes and substrates strictly follow the respective regularity independently. Atomically sharp interfaces are formed at morphotropic GBs between homogenetic layers with different orientations and strain states. The atomic-thin GBs naturally isolate the distinct regions with strikingly different electronic states and magnetic behavior in hybrid structures, enabling artificially engineered functionalities in the planar matrix. The ability to fine-tune lateral structure-driven functional properties demonstrates a practical path toward the rational design of magnetoelectric and spintronic logic devices, as well as microscopic surface catalysis.

2. Results

The water-soluble sacrificial strontium aluminate (Sr₃Al₂O₆) layer (≈30 nm) and a subsequent ultrathin SrTiO₃ (STO) layer (≈3 nm) were grown on a (001)-oriented (LaAlO₃)_{0.3}–(Sr₂AlTaO₆)_{0.7} (LSAT) single-crystalline substrate using the pulsed laser deposition (PLD) technique. Then, the STO layer was attached to a thermal-release tape and delaminated from LSAT substrates after dissolving the sacrificial layer in deionized water.^[24–26] The released single-crystalline STO membranes with step-and-terrace morphology were transferred onto the target substrates (see Experimental Section and Figure S1, Supporting Information). The STO membranes maintain their shape and crystalline quality in millimeter size. We did not cover the entire surface of the substrates with the STO membranes to allow subsequent thin layers to be epitaxially grown on both regions simultaneously. The area ratio between STO membranes and substrates was 1:3. We chose La_{0.8}Sr_{0.2}CoO₃ (LSCO) as a model system because its specific Sr composition is close to the phase boundary, where small structural perturbations significantly change its physical properties.^[27] LSCO layers with a thickness of ≈30 nm were grown on the modified substrates. A representative hybrid structure composed of (001)- and (110)-oriented LSCO layers on (110)-STO substrates is displayed in **Figure 1a**. X-ray diffraction (XRD) measurements confirm the epitaxial growth of LSCO layers with both (00*l*) and (*l*0) reflections (**Figure 1b** and **Figure S2**, Supporting Information). The crystalline structure of the (001)-STO mem-

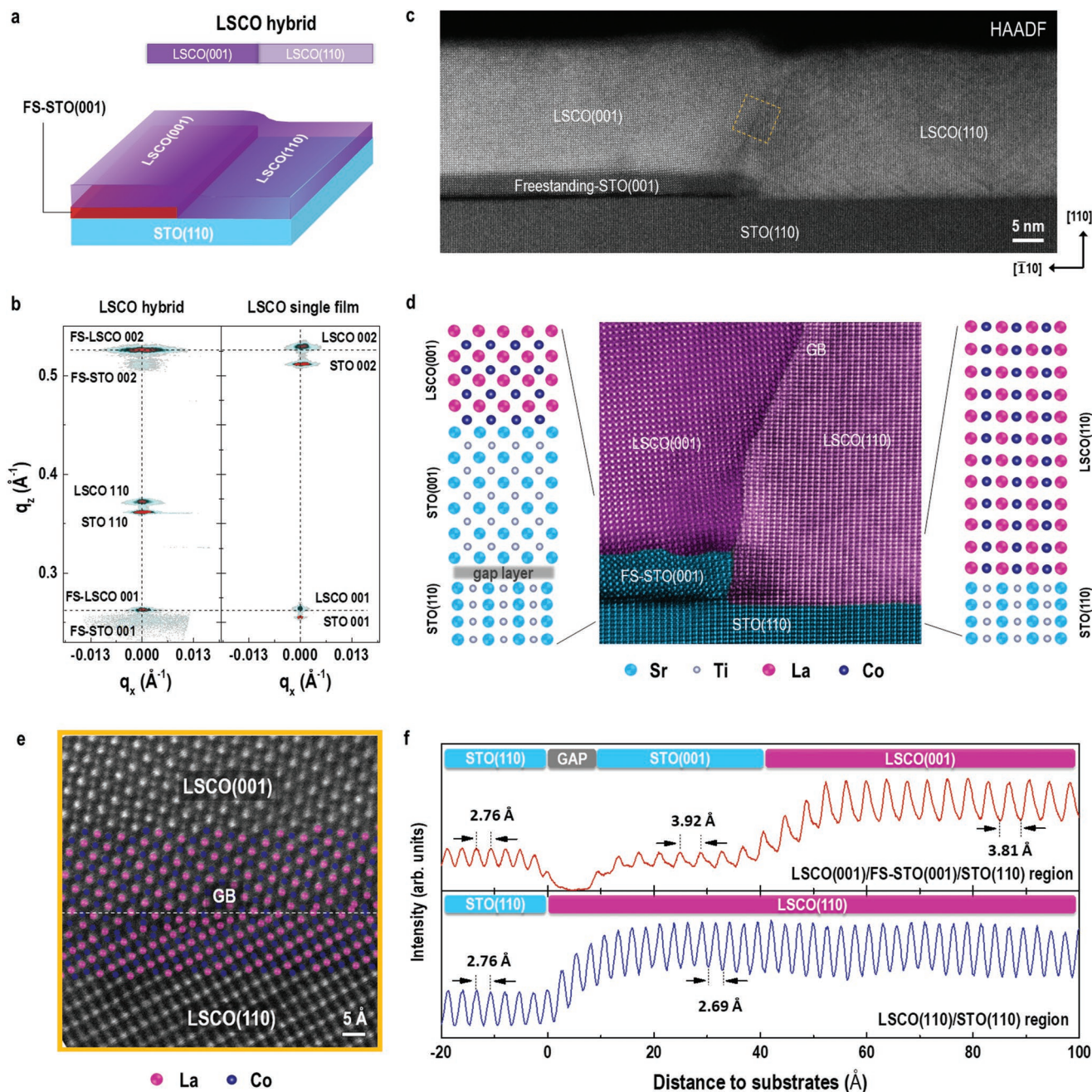


Figure 1. Structural characterization of a LSCO hybrid structure with morphotropic grain boundaries. a) Schematic of a lateral homogenetic LSCO hybrid structure. The LSCO layers grown on (110)-oriented STO substrates maintain the substrate's orientation, whereas the LSCO layers follow the orientation of (001)-oriented freestanding (FS)-STO membranes underneath. b) Reciprocal space map (RSM) of a LSCO hybrid structure and a (001)-oriented LSCO single layer around the substrates' (110) reflection. Both (001) reflections from FS-STO and LSCO layers are observed besides the typical (110) reflections from the LSCO film and substrates. c) Cross-sectional high-angle annular dark-field (HAADF) STEM images of a LSCO hybrid structure. d) A high-magnification STEM image around morphotropic grain boundary. The atomic arrangements at two representative regions are present for clarification. e) An atomic-resolved STEM image around grain boundary between (001)- and (110)-oriented LSCO layers, demonstrating the atomically sharp interfaces with minimal dislocations and cation defects. f) Intensity profiles obtained from line scans averaged across the respective regions in (d).

branes is preserved, and these membranes act as a template for subsequent LSCO layer growth. Conversely, the ultrathin STO membranes render them responsive to compressive strain from the top LSCO layers. The out-of-plane lattice constant of the (001)-LSCO layer ($\approx 3.81 \text{ \AA}$) grown on STO membranes

is larger than that of a coherently strained (001)-LSCO single film ($\approx 3.77 \text{ \AA}$), implying that the lattice structure of the LSCO layer is slightly relaxed. The atomic-scale structural coherency of LSCO hybrid structures grown on (110)-oriented STO substrates was examined by cross-sectional high-angle annular

dark-field (HAADF) imaging via scanning transmission electron microscopy (STEM) (Figure 1c and Figure S3, Supporting Information). The ultrathin STO membranes with a thickness of ≈ 8 unit cells are continuous, atomically smooth and free from chemically intermixing or defect formation after release, transfer and post-synthesis (Figure S4, Supporting Information). The extremely narrow gap (≈ 1 nm on average) between the STO membranes and substrates is naturally formed (Figure S5, Supporting Information). Most STO membranes are chemically unbonded with substrates because of the crystallographic orientation mismatch and polar interface. Atomic-resolution STEM images of an LSCO hybrid structure in different regions (Figure 1d and Figure S6, Supporting Information) show that LSCO layers strictly follow the orientations of STO membranes and substrates. The schematic of the atomic structure shown in Figure 1d manifest the epitaxial relationship across the distinct LSCO/STO interfaces. Figure 1e shows a HAADF-STEM image of the GB between homogenous LSCO layers with different orientations. Notably, the GB has an atomically sharp interface with a highly periodic configuration of atoms due to energy minimization to misfit strain and different crystallographic facets. Figure 1f shows the averaged atomic intensities in the HAADF-STEM image at different interface regions (Figure 1e). This qualitative analysis enables the precise realization of out-of-plane lattice constants of each layer. We also performed a geometric phase analysis (GPA) of HAADF-STEM images across the LSCO/STO interfaces (Figure S7, Supporting Information). Similar to the coherently epitaxial growth of (110)-LSCO layers on STO substrates, the (001)-LSCO layers have an identical in-plane lattice constant but a smaller out-of-plane lattice constant than those of STO membranes. The top LSCO layer compresses the STO membranes along the in-plane direction, increasing the out-of-plane lattice constant, compared with the STO bulk. The STEM results confirm the structural relaxation of (001)-LSCO layers on STO membranes, which is consistent with XRD measurements. Furthermore, following the same protocol, we successfully constructed a similar hybrid structure consisting of (001)- and (111)-oriented LSCO layers on (111)-STO substrates (Figure S8, Supporting Information), confirming that our methodology for fabricating homostructures with lateral GBs is universal and highly reproducible.

In addition to the detailed analysis of structural evolution and GBs, we investigated the transport and magnetic properties of LSCO hybrid structures using (110)-STO substrates. For a (001)-LSCO/STO freestanding (FS) membrane attached to PDMS support, the in-plane saturation magnetization (M_S) is ≈ 200 emu cm^{-3} and the coercive field (H_C) is ≈ 5 kOe at 10 K (Figure 2a). M_S reduces to 85 emu cm^{-3} and H_C increases to ≈ 8 kOe when an LSCO single film is grown on (110)-STO substrates (Figure 2b). A strong reduction in the ordered magnetic moment with increasing tensile strain is consistent with earlier work.^[28] The decrease in M_S is irrelevant to the change in Co covalence and spin state because the tensile strain increases the magnetic moment in undoped cobaltite films.^[29] We observed a two-step switching in the magnetic hysteresis loop of an LSCO hybrid structure grown on (110)-STO substrates (Figure 2c), implying that the (001)-STO and (110)-STO layers respond differently to the applied fields. Figure 1d shows temperature-dependent resistivity (ρ) in a (001)-FS-LSCO, a (110)-LSCO

single layer, and an LSCO hybrid structure. (001)-FS-LSCO is highly insulating, with its ρ exceeding the measurement limit at room temperature ($\rho_{300\text{K}} > 100 \Omega \text{ cm}$). The ρ of an LSCO hybrid structure is smaller than that of a (110)-LSCO single film, exhibiting a typical resistivity property of the parallel-connected circuit. The temperature-dependent magnetization (M) at an in-plane field of 1 kOe exhibits nearly identical $T_C \approx 195$ K for all three samples (Figure 1e). The M of an LSCO hybrid structure is larger than that of a (110)-LSCO single layer but smaller than that of a (001)-FS-LSCO. Figure 2f,g shows the field-dependent magnetoresistance $[(\rho_H - \rho_0)/\rho_0]$ and M of an LSCO hybrid structure at various temperatures. $(\rho_H - \rho_0)/\rho_0$ and the magnetic field at peak positions (corresponding to H_C) reduce progressively with increasing temperature, revealing a typical ferromagnetic characteristic. The double hysteresis loop in LSCO hybrid structures disappears when T exceeds 100 K. This fact suggests that, at high temperatures, the magnetic contribution from (110)-STO layers is negligible, and (001)-FS-LSCO layers dominate the total magnetization of an LSCO hybrid structure. In addition, similar field-dependent magnetization was observed in LSCO hybrid structures on (111)-STO substrates (Figure S9, Supporting Information). These findings show that LSCO layers with different orientations embedded in a single hybrid structure have unique physical properties and regions separated by lateral GB responses that are independent of external fields.

To verify that our method can be universally used to create GBs between oxide layers with different strain states, we grew LSCO hybrid structures on STO-membrane-covered LaAlO_3 (LAO) and KTaO_3 (KTO) substrates with a (001) orientation, respectively. The in-plane strain of LSCO layers varies from compressive (approximately -1.25% on LAO) to tensile ($\approx 1.7\%$ on STO and -4% on KTO) depending on substrates. We first verified that a compressively strained LSCO single film on LAO undergoes an insulator-to-metal transition at ≈ 175 K (confirmed by the first derivation of $\rho-T$ curve), whereas the tensile-strained LSCO films on STO and KTO exhibit insulating behavior at all temperatures (Figure S10, Supporting Information). M_S at 10 K under a magnetic field of 7 T decreases significantly with increasing in-plane lattice parameters. Through polarized neutron reflectometry, we also confirm that the magnetization of an LSCO single film is uniform across the entire sample and only a small variation (less than 5%) exists at the surface and interface (Figure S11, Supporting Information) due to the different boundary conditions.^[30] Therefore, LSCO is an excellent candidate for manipulating strain-driven electronic and magnetic properties across GBs. Figure 3a shows a high-resolution HAADF-STEM image across interfaces between LSCO layers, FS-STO membranes, and LAO substrates. The [010] orientation of FS-STO membranes is twisted $\approx 16^\circ$ with respect to the [010]_{pc} orientation of LAO substrates (Figure S12, Supporting Information), which is confirmed by the atomic-resolution STEM image from top LSCO/STO layers, but well-aligned atomic planes at LAO substrates. From geometric phase analysis (GPA) and line profiles across heterointerfaces, the lattice constants of LSCO layers can be accurately obtained (Figure 3b,c and Figure S13, Supporting Information). Both LSCO layers are coherently grown on both LAO substrates and STO membranes. The LSCO layers undergo compressive strain

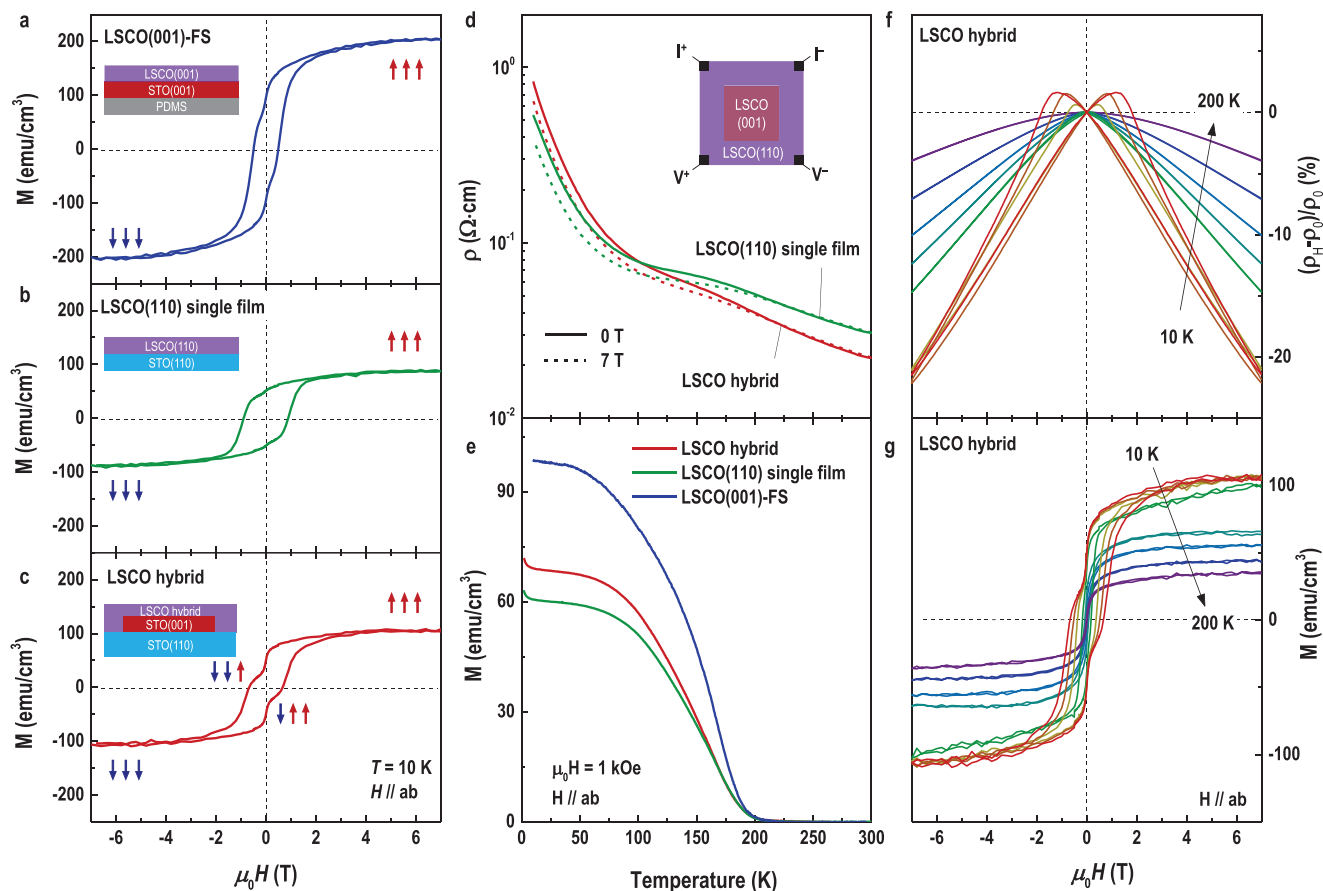


Figure 2. Magnetometry and transport measurements on LSCO hybrid structures. a–c) Field-dependent magnetization of a (001)-oriented FS-LSCO membrane (a), a (110)-oriented LSCO single film (b), and a LSCO hybrid structure grown (c) on (110)-STO substrates. The magnetic field was applied along the in-plane direction. The M – H loops were measured at 10 K. Apparently, the M – H loop of a LSCO hybrid structure is the superposition of those from a (001)-oriented FS-LSCO membrane and a (110)-oriented LSCO single layer. d,e) Temperature-dependent resistivities (ρ) (d) and magnetization (e) of a (110)-oriented LSCO single film and a LSCO hybrid structure on (110)-STO substrates. ρ – T curves were measured at 0 and 7 T. M versus T scans were collected during sample warming after field-cooling at 1 kOe. f,g) Field-dependent magneto-resistance [$(\rho_H - \rho_0)/\rho_0$] (f) and magnetization (g) of a LSCO hybrid structure at various temperatures ranging from 10 to 200 K.

caused by LAO, whereas they are slightly tensile-strained by STO membranes. The STO membranes are conversely in-plane compressed by LSCO top layers, resulting in a slightly higher out-of-plane lattice constant (≈ 3.92 Å) than its bulk value.

Distinct strain states of LSCO layers in different regions would induce significant lateral modulation in the orbital occupancy of valence electrons. We performed elemental-specific X-ray absorption spectroscopy (XAS) at Co L -edges on an LSCO hybrid structure. XAS measurements were conducted at 77 K under a zero magnetic field, ensuring that XAS reflects the genuine electronic occupancy of Co d orbitals. Figure 3d shows the experiment configuration for XAS measurements at the edge (LSCO/LAO) and center (LSCO/STO) regions of an LSCO hybrid structure. By detecting the absorption of linearly polarized X-rays with different incident angles (I_{0° and I_{60°), we could probe the respective energies and unoccupied states, that is, holes, in the Co $d_{x^2-y^2}$ and $d_{3z^2-r^2}$ orbitals (Figure S14, Supporting Information). X-ray linear dichroism (XLD) spectra were quantified by calculating the difference between I_{0° and I_{60° , directly reflecting the orbital polarization in different regions of an LSCO hybrid structure. As shown in Figure 3e,

XLD spectra from edge and center regions of an LSCO hybrid structure on LAO exhibit an obvious sign reversal. Compressive strain-induced orbital splitting results in low energy and highly occupied $d_{3z^2-r^2}$ orbitals, whereas tensile strain has the opposite effect. Furthermore, the XLD of an LSCO hybrid structure on KTO confirms that electrons preferentially occupy the $d_{x^2-y^2}$ orbitals when LSCO layers are tensile-strained by STO membranes or KTO substrates (Figure S14, Supporting Information). The XLD results are consistent with those obtained for LSCO single films grown on the respective substrates (Figure S15, Supporting Information), showing that strain-driven orbital occupancy switching is robust.^[31] These observations provide strong evidence that lateral strain modulation induces significant in-plane anisotropy in the electronic configuration, affecting both band splitting and orbital polarization in Co d bands.

The effects of lateral strain modulation and GBs on the electric and magnetic properties of LSCO hybrid structures were further investigated by DC transport measurements. Magneto-resistance and Hall conductivity were measured at the edge (Figure 4a) and center (Figure 4b) regions of an LSCO hybrid

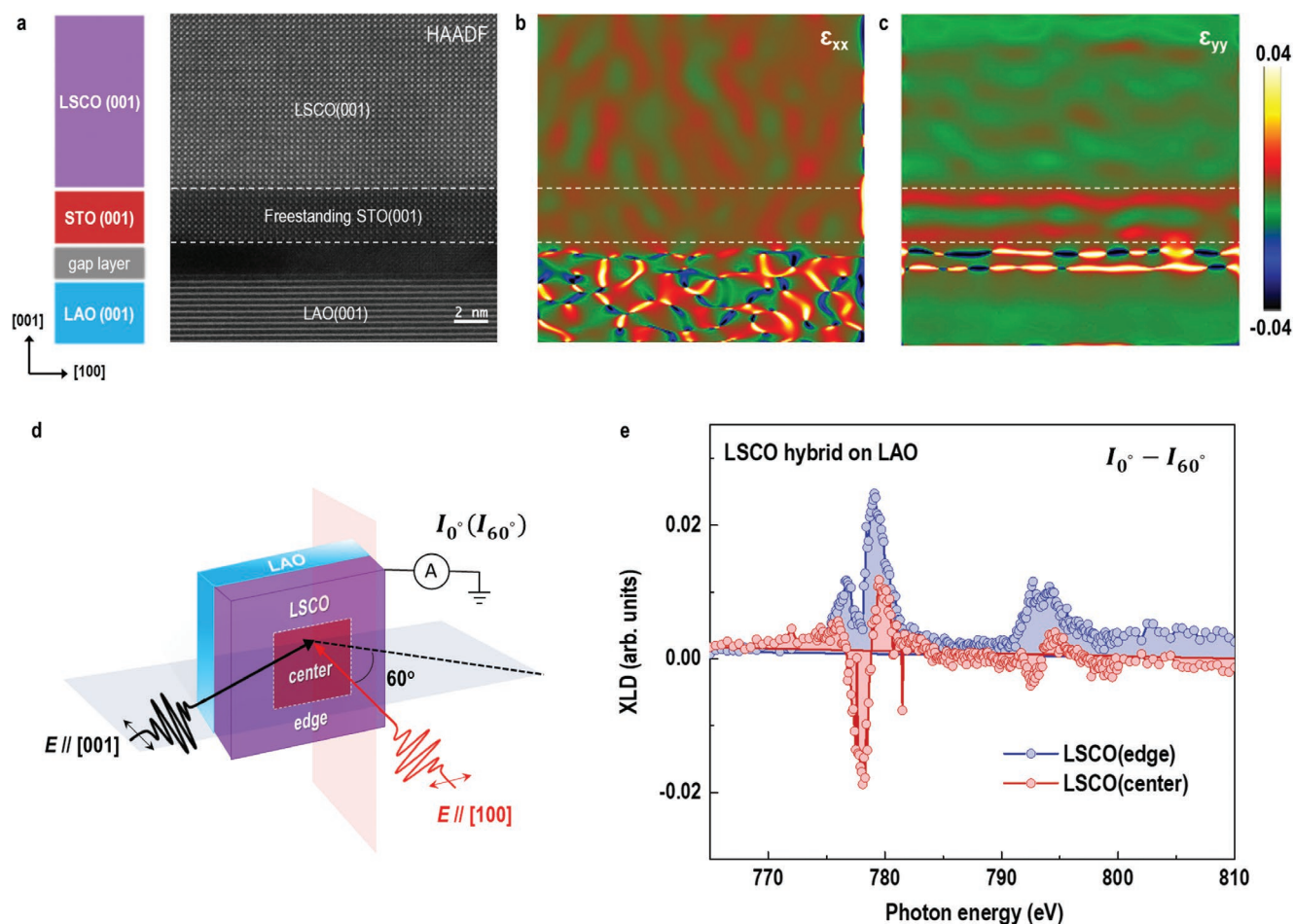


Figure 3. Strain-mediated orbital polarization in LSCO hybrid structures. a) Schematic and HAADF-STEM image of a LSCO hybrid structure grown on (001)-oriented LAO substrates. b) In-plane and c) out-of-plane strain distributions within the LSCO hybrid structures performed by geometric phase analysis (GPA). d) Schematic of the scattering geometry for XAS measurements with X-ray beam aligned parallel (0°) or with an angle of 60° with respect to the surface normal. X-ray linear dichroism (XLD) spectra were quantified by calculating the difference between I_{0° and I_{60° . e) XLD of LSCO hybrids on LAO substrates, respectively. XLD spectra from the edge and center regions of LSCO hybrids show the distinct differences, indicating that the hole occupancy in the 3d orbitals from these regions are in sharp contrast. The degree of orbital polarization exhibits a clear anisotropic orbital occupancy depending on the strain states of LSCO hybrids. All spectra were collected around Co *L*-edges at 77 K in TEY mode.

structure independently (Figures S16 and S17, Supporting Information). Temperature-dependent ρ of LSCO hybrid structures exhibit a semimetallic behavior with a local maximum at ≈ 170 K, corresponding to the magnetic phase transition temperature. Comparing this behavior with an LSCO single film on LAO, we observe quantitatively similar temperature-dependent resistivity that is roughly an order of magnitude larger than LSCO hybrid structures. This is due to the highly insulating state in tensile-strained LSCO layers on STO membranes, leading to finite electrical conductivity. The Hall measurements of LSCO hybrid structures led to an unprecedented observation. Above T_C , the Hall response is approximately linear with a positive slope, indicating *p*-type carriers. At low temperatures, a nonlinear anomalous Hall effect (AHE) appears, opening a large hysteresis loop with a shape and coercive field practically identical to *M*–*H* sweeps. When *T* is below 30 K, the anomalous Hall effect (AHE) disappears. Figure 4c,d shows direct comparisons of anomalous Hall resistivity ($\rho_{xy} - R_0H$) in different regions as a function of magnetic field and temperature,

respectively. At 50 K, $\rho_{xy} - R_0H$ (edge region) has a square-like loop, whereas $\rho_{xy} - R_0H$ (center region) has negligible values. $\rho_{xy} - R_0H$ reaches a maximum (minimum) value at 100 K when measured at edge (center) regions; however, the numerical sign of $\rho_{xy} - R_0H$ is the opposite. In addition, the magnetoresistance of LSCO hybrid structures at both edge and center regions has negligible values at high temperatures. A negative response starts to appear near and below the T_C and increases systematically in magnitude with decreasing temperature. When *T* is below 100 K, the butterfly hysteresis loop appears in the small field that is coupled with H_C . Figure 4e,f plots field- and temperature-dependent magnetoresistance recorded in different regions, respectively. They show a distinct response to the applied field below T_C , indicating that the onset of magnetization in LSCO hybrid structures is laterally different.

The direct evidence of the magnetic contrast across the GB is provided by nanodiamond (ND) nitrogen vacancy (NV) magnetometry measurements at the edge and center regions of an LSCO hybrid structure on LAO substrates. NV magnetometry

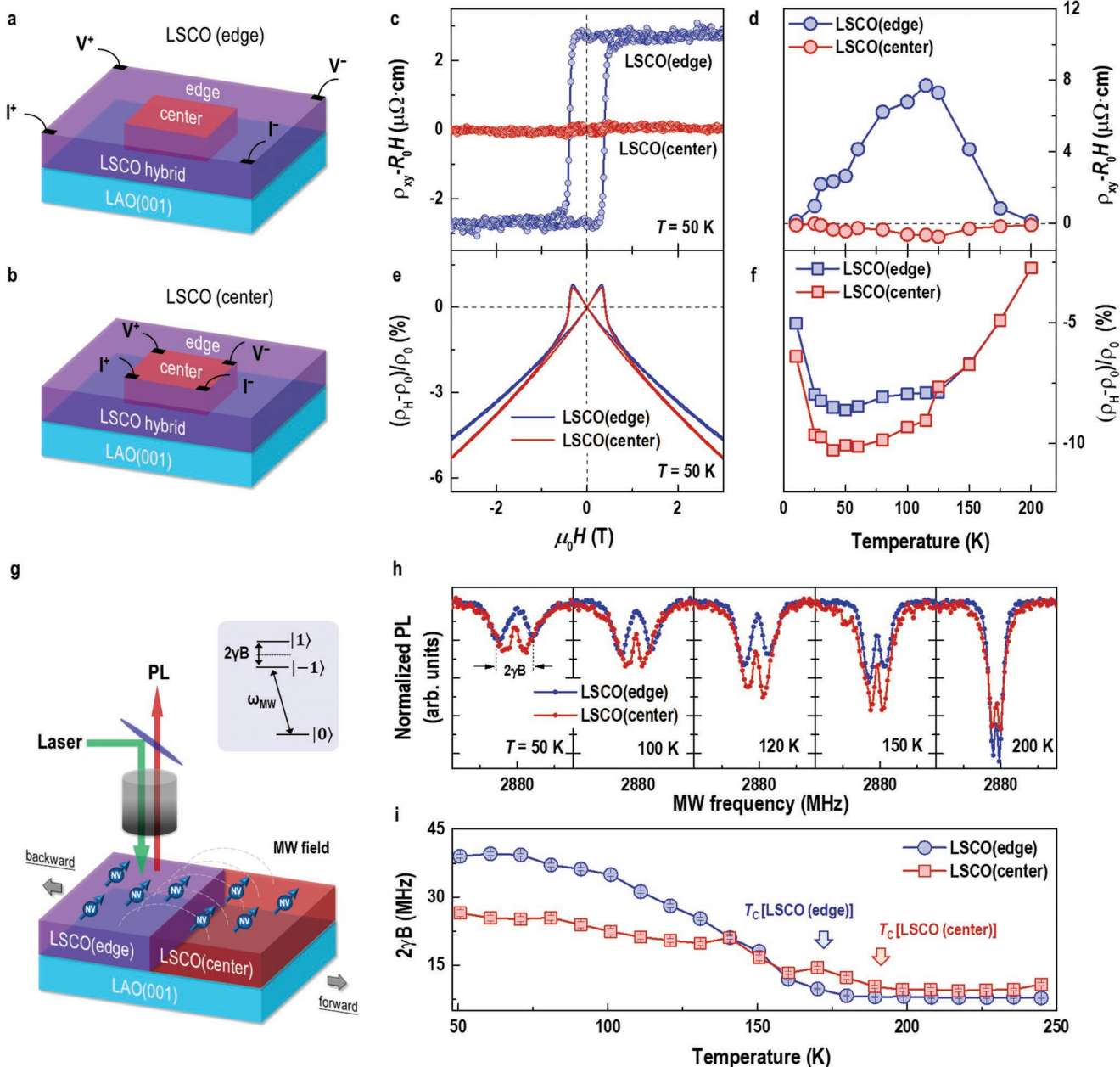


Figure 4. Distinct ground states across grain boundary in LSCO hybrid structures. (a) and (b) schematic setups for transport measurements at the LSCO (edge) and LSCO (center) regions, respectively. c,e) Field-dependent anomalous Hall resistivity ($\rho_{xy} - R_0H$) (c) and magnetoresistance $[(\rho_H - \rho_0)/\rho_0]$ (e) measured at the LSCO (edge) and LSCO (center) regions at 50 K. R_0H represents the ordinary Hall term that is subtracted from ρ_{xy} by linearly fitting the data at high magnetic field region. d,f) Temperature dependent $\rho_{xy} - R_0H$ (d) and $(\rho_H - \rho_0)/\rho_0$ (f) measured at the LSCO (edge) and LSCO (center) regions when $\mu_0H = 7$ T. g) Schematic of diamond NV-based magnetometry performed at different regions of LSCO hybrid structures grown on LAO substrates. h) Zero-field optically detected magnetic resonance (ODMR) spectra of NV centers dispersed randomly on the surface of LSCO hybrid structures. The ODMR spectra were collected at different temperatures (extended data Figure S18, Supporting Information). i) Temperature dependence of $2\gamma B$ for LSCO (edge) and LSCO (center) regions, which exhibit different magnetic phase transition temperatures.

was performed in zero magnetic fields and at fixed temperatures ranging from 50 to 250 K. By recording optically detected magnetic resonance (ODMR) spectra of NV centers, we could calculate the projection of the magnetic stray field that originated from LSCO layers along the NV axis because $M_s = \pm 1$ sublevels undergo energy splitting ($2\gamma B$) in the presence of weak magnetic perturbation (B) (Figure 4g). Figure 4h and Figure S18,

Supporting Information, depict ODMR spectra of a single ND dispersed on the surface of edge and center regions at various temperatures. At 50 K, the splitting between two resonant peaks is significant, indicating the existence of measurable remnant magnetization in LSCO layers. The splitting becomes narrow and reaches a saturated minimum value as temperature increases. We calculated $2\gamma B$ by subtracting two resonant peak

frequencies after Gaussian fitting to ODMR spectra. Figure 4i shows temperature-dependent $2\gamma B$ measured at the edge and center regions of LSCO hybrid structures. The magnitude of $2\gamma B$ depends on multiple factors, including the number of NVs in a single ND, proximity distance and magnetic homogeneity. Thus, the quantitative comparison of $2\gamma B$ obtained from different regions is challenging. However, the magnetic phase transition temperatures of LSCO layers at edge and center regions are significantly different. LSCO (edge) layers on LAO substrates have a lower T_C than LSCO (center) layers on STO membranes. These measurements were repeated randomly using different NDs in each region. The trend in magnetization obtained from NV magnetometry correlates with $M-T$ curves from macroscopic magnetometry results on LSCO single films and LSCO/STO membranes (Figure 2e and Figures S9 and S10, Supporting Information), corroborating the lateral magnetic anisotropy of LSCO hybrid structures with different strain states isolated by GBs.

3. Discussion and Conclusions

So far, we have demonstrated the creating of lateral GBs in ferromagnetic LSCO hybrid structures with different crystallographic orientations and strain states. By designing and artificially engineering GBs in a controlled way, this work may also open all kinds of interesting fundamental and applied research out of quantum materials. The results are highly reproducible, and most importantly, the growth sequence can be reversed (Figure S19, Supporting Information). For instance, we fabricated (110)- and (111)-oriented STO membranes and attached them to (001)-STO substrates. Hence, LSCO hybrid structures were formed on (001)-STO substrates, which exhibit similar magnetic contrast laterally. In principle, the freestanding membranes (not limited to STO used in this study) can be transferred onto arbitrary substrates, such as metals, semiconductors, as well as amorphous glass, which is crucial for fabricating complex laterally hybrid structures with emergent physical properties (Figure S19, Supporting Information). Furthermore, we also show the successful control of membrane's orientation with respect to the substrate (Figure S20, Supporting Information). The LSCO layers strictly follow the orientation of freestanding membrane/substrate, allowing the possible design of GB with arbitrary orientations and types. This work can be applied to a broad range of applications. First, the size of membranes can be reduced to a nanometer scale using a sacrificed nanoporous anodic alumina template or through UV lithography post-synthesis.^[32] The arrayed nanodots enable on-demand manipulation of topological nanoripples, spin-textured domains, or multiferroic vortices. Second, the creation of GBs composed of unique periodic arrangements of structural units in any single-crystalline oxide is achievable and accurately adjustable by a function-driven design. The type, density, and location of GBs are highly controllable. Tunability via GB engineering with broken inversion symmetry may open vistas in nanoelectronics and nanoelectromechanical systems.^[33] Last but not the least, the proposed technique enables the stacking of correlated oxide membranes with precisely controlled twisted angles with respect to subsequent-grown

layers, mimicking twistrionics in 2D materials.^[34] This method advances our ability to minutely engineer functional properties by lateral homoepitaxy of strongly correlated materials that drive many intriguing behaviors, such as superconductivity, multiferroicity and magnetic textures, across multiple length scales, and is readily applied to the imperative fields of neuro-morphics, solid-state batteries, catalysis, etc.

4. Experimental Section

Synthesis of LSCO Hybrid Structures: The water-soluble $\text{Sr}_3\text{Al}_2\text{O}_6$ (SAO) and SrTiO_3 (STO) layers were grown subsequently on (001)-oriented $(\text{LaAlO}_3)_{0.3}-(\text{Sr}_2\text{AlTaO}_6)_{0.7}$ (LSAT) substrates (Hefei Kejing Mater. Tech. Co. Ltd) by PLD technique. A focused XeCl excimer laser with duration of ≈ 25 ns, fixed wavelength of 308 nm, and energy density of ≈ 1.5 J cm⁻² was used as the ablation source. The bilayers were deposited at the substrate temperature of 800 °C and oxygen partial pressure of 50 mTorr. The thicknesses of SAO and STO layers were ≈ 30 and ≈ 3 nm (≈ 8 unit cells, u.c.), respectively. On the completion of epitaxy, the STO/SAO bilayers were cooled down to room temperature at the growth pressure. The morphology of as-grown STO/SAO bilayer was checked by AFM, demonstrating a step-and-terrace structure. A thermal-release tape (or a PDMS, PF-40-X4, Gel-Pak) was pressed firmly on the as-grown sample and then immersed into deionized water at room temperature (Figure S1, Supporting Information). After the water-soluble SAO layer was fully dissolved, the ultrathin STO membrane was adhered on the thermal-release tape (or a PDMS). Afterward, the tape-supported STO membranes were transferred on the target substrates, for instance the (110)- and (111)-oriented STO, LaAlO_3 (LAO), KTaO_3 (KTO) and SiO_2/Si substrates, followed by peeling off the thermal-release tape by heating at ≈ 90 °C for 10 min. After that, the ultrathin STO membranes remained on the target substrates after detaching the supports. Subsequently, the $\text{La}_{0.8}\text{Sr}_{0.2}\text{CoO}_3$ (LSCO) thin films with a thickness of ≈ 30 nm were fabricated on the prepared substrates by PLD. The thickness of LSCO films was carefully selected by keeping them coherently grown on different target substrates. The LSCO films exhibit distinct physical properties depending on the crystallographic orientation and misfit strain. During the growth of LSCO layers, the substrate temperature was kept at 750 °C and oxygen partial pressure was maintained at 200 mTorr. After the deposition, the samples were cooled down under the oxygen pressure of 100 Torr. The post-oxygen annealing process prevented the formation of oxygen vacancies in the LSCO films, which are well-known to affect their intrinsic physical properties.^[35,36]

Structural Characterizations: Crystallographic analysis, that is, X-ray diffraction $2\theta-\omega$, X-ray reflectivity (XRR), and reciprocal space mapping (RSM), were carried out using a Panalytical X'Pert3 MRD diffractometer with $\text{Cu } K\alpha_1$ radiation equipped with a 3D pixel detector. The thicknesses of layers were obtained by fitting XRR curves using GenX software.^[34] The growth rate of each layer was calculated and controlled precisely by counting the number of laser pulses. Cross-sectional TEM specimens of LSCO hybrid structures with different crystallographic and strain states were prepared using Ga^+ ion milling after the mechanical thinning. The HAADF and ABF imaging were performed in the scanning mode using JEM ARM 200CF microscopy at the Institute of Physics (IOP), Chinese Academy of Sciences (CAS). For some cases, the [100] zone axis of STO(001) membranes was not well aligned with $[\bar{1}\bar{1}0]$ or $[1\bar{1}\bar{2}]$ zone axis of STO(011) or STO (111) substrates, respectively. The LSCO hybrid specimens need to rotate by a few degrees along the in-plane direction in order to obtain the atomic-precision images from different regions. The atomic positions of cations were determined by fitting the intensity peaks with Gaussian function. The obtained values were used to calculate the lattice parameters of each layer. The error bars were extracted by calculating the standard deviation value. The elemental specific electron energy loss spectra (EELS) mappings were performed by integrating the signals from a selected region after subtracting the

exponent background using power law. All data were analyzed using Gatan Micrograph software.

Electrical Transport and Magnetization Measurements: The macroscopic magnetizations of LSCO hybrid structures were measured by a 7 T–MPMS magnetometer. All measurements were performed by applying magnetic fields up to ± 7 T. The M – T curves were recorded during the sample warm-up process after field-cooled at 1 kOe. The M – H hysteresis loops up to ± 7 T were recorded at different temperatures. The M – H loops were obtained by subtracting the diamagnetic signals from the STO membranes and substrates. The magnetization of LSCO hybrid structures were normalized to the thickness of LSCO layers. The electrical transport measurements were conducted by a 7 T–PPMS. The resistivities and Hall conductivities were measured using the standard van der Paw method.

Spectroscopic Characterizations: Elemental specific XAS measurements were performed on the LSCO hybrid structures grown on LAO and KTO substrates at the MCD beamline of National Synchrotron Radiation Laboratory (NSRL) in Hefei, China. All spectra at the Co L -edges were collected at 77 K in total electron yield (TEY) mode. Although the LSCO films stay in the insulating states, the resistivities of LSCO stay in the order of kilohm range. Meanwhile, our samples were properly electrically connected to the sample holder using silver glue. The conductivities of measured layers allow the steady measurements with photocurrent in tens of picoamperes. A severe charge effect during the measurement was not observed. The XLD measurements were performed by changing the incident angle of the linearly polarized X-ray beam. The X-ray scattering plane was rotated by 0° and 60° with respect to the incoming photons. The XAS signals were normalized to the values at the pre- and post-edges. When the X-ray beam was perpendicular to the surface plane (0°), XAS signal directly reflects the $d_{x^2-y^2}$ orbital occupancy. While the angle between the X-ray beam and surface plane was 60° , the XAS signal contains orbital information from both $d_{x^2-y^2}$ and $d_{3z^2-r^2}$ orbitals. For simplifying the discussions, the XLD signals of LSCO hybrid structures were calculated by $I_{0^\circ} - I_{60^\circ}$. The XLD signal directly reflects the orbital polarization of a sample under different strain states.^[35]

Diamond NV-Based Magnetometry: The diamond nitrogen vacancy (NV)-based magnetometry measurements were performed at zero magnetic field using a home-built ODMR system.^[36] Nanodiamonds (NDs) with a nominal diameter of ≈ 100 nm and typically ≈ 500 NV centers per crystal were used (Adamas Nanotechnologies) as spin sensors. The NDs on the surface of LSCO hybrid structures were dispersed randomly with a low density so that the individual NDs could be addressed and probed with the confocal microscope. The ODMR spectra were taken by sweeping the microwave frequency through resonance and recording the photon excitations from the NDs. The ground states of NV center were spin-1 and there was only one resonant dip at 2870 MHz at zero magnetic field ($m_s = \pm 1$ states were degenerated) and room temperature. If a stray field was generated by the LSCO hybrids, the ODMR spectrum of an NV center splits into two dips due to the Zeeman effect. The amplitude of spectral splitting was in proportion to the strength of the stray field. Thus, the local field strength was extracted from the width of single-peak Lorentz fitting. Please note that there were hundreds of NV centers in a single ND and the stray field might have a gradient at the 100 nm scale, thus the ODMR spectra of NDs from our LSCO hybrids were broadened as compared to that of a single NV center. The samples were pasted on a cooling stage attached to a closure He-recycling refrigerator. The temperature of the samples was controlled between 10 to 300 K and monitored using a conventional thermometer attached on the sample stage. The cooling stage could be moved precisely at the micrometer scale, so that the ODMR spectra and their temperature dependencies from different regions of a LSCO hybrid structure could be obtained separately.

Nanoscale Magnetization Profiling Using PNR: The PNR experiment on a LSCO single film grown on the LAO substrate was performed at the Multipurpose Reflectometer (MR) of Chinese Spallation Neutron Source, Dongguan, China. The sample was measured at 10 K under an in-plane magnetic field of 1 T. PNR measurements were conducted in the

specular reflection geometry with wave vector transfer (q) perpendicular to the surface plane. q is calculated by $4\pi \sin(\alpha_i)/\lambda$, where α_i is the neutron incident angle and λ is the wavelength of neutron beam. The neutron reflectivities from spin-up (R^+) and spin down (R^-) neutrons were recorded separately. The spin asymmetry (SA) was calculated using $(R^+ - R^-)/(R^+ + R^-)$. By fitting the PNR data, the magnetization and nuclear scattering length density profiles of LSCO layers was obtained simultaneously. The standard deviations of the magnetization values form the uncertainties of the M_s .

Supporting Information

Supporting Information is available from the Wiley Online Library or from the author.

Acknowledgements

The authors thank Xiahan Sang, T. Zac Ward, Michael R. Fitzsimmons, Sujit Das, Guoqiang Yu, Yu Ye, Qian Li, Hangwen Guo and Qiyang Lu for valuable discussions, as well as Tengyu Guo and Baoshan Cui for the extensive assistance in the magnetization measurements at SLAB. Funding Sources: This work was supported by the National Key Basic Research Program of China (Grant Nos. 2020YFA0309100 and 2019YFA0308500), the National Natural Science Foundation of China (Grant Nos. 11974390, 11721404, 12174364, 11874412, and 12174437), the Beijing Nova Program of Science and Technology (Grant No. Z191100001119112), the Beijing Natural Science Foundation (Grant No. 2202060), the Guangdong-Hong Kong-Macao Joint Laboratory for Neutron Scattering Science and Technology, the Strategic Priority Research Program (B) of the Chinese Academy of Sciences (Grant No. XDB33030200), Excellence Program of Hefei Science Center CAS (No. 2021HSC-UE003), and the Fundamental Research Funds for the Central Universities (No. wk2310000104). The XAS and XLD experiments were conducted at the National Synchrotron Radiation Laboratory (NSRL) in Hefei, China via a user proposal.

Conflict of Interest

The authors declare no conflict of interest.

Author Contributions

S.C., Q.Z., and D.R. contributed equally to the manuscript. The LSCO samples were grown and processed by S.R.C. under the guidance of E.J.G., and the SAO samples were fabricated by J.F.Z. under the guidance of L.F.W.; the transfer of freestanding oxide membranes was conducted by D.K.R.; XAS and XLD measurements were performed by F.F.P., Q.L., and W.S.Y.; the NV magnetometry was performed by Y.X., Y.X.S., and G.Q.L.; TEM lamellas were fabricated with FIB milling and TEM experiments were performed by Q.H.Z. and L.G.; PNR measurements were performed by H.B. and T.Z.; S.R.C., S.L., Q.J., and H.T.H. worked on the structural and magnetic measurements. C.W. and H.G. participated in the discussions and K.J.J. provided important suggestions during the manuscript preparation. E.J.G. initiated the research and supervised the work. S.R.C. and E.J.G. wrote the manuscript with input from all authors.

Data Availability Statement

The data that support the findings of this study are available from the corresponding author upon reasonable request.

Keywords

cobaltites, freestanding membranes, grain boundaries, lateral homostructures, oxide interfaces

Received: July 31, 2022
Revised: October 14, 2022
Published online:

- [1] J. Mannhart, D. G. Schlom, *Science* **2010**, 327, 1607.
- [2] J. Chakhalian, A. J. Millis, J. Rondinelli, *Nat. Mater.* **2012**, 11, 92.
- [3] H. Y. Hwang, Y. Iwasa, M. Kawasaki, B. Keimer, N. Nagaosa, Y. Tokura, *Nat. Mater.* **2012**, 11, 103.
- [4] A. Ohtomo, D. A. Muller, J. L. Grazul, H. Y. Hwang, *Nature* **2002**, 419, 378.
- [5] J. Mannhart, D. H. A. Blank, H. Y. Hwang, A. J. Millis, J. M. Triscone, *MRS Bull.* **2008**, 33, 1027.
- [6] H. Hilgenkamp, J. Mannhart, *Aspects Med. Phys., Rev. Pap. Int. Conf., 1st* **2002**, 74, 485.
- [7] C. Sohn, E. Skoropata, Y. Choi, X. Gao, A. Rastogi, A. Huon, M. A. McGuire, L. Nuckols, Y. Zhang, J. W. Freeland, D. Haskel, H. N. Lee, *Adv. Mater.* **2019**, 31, 1805389.
- [8] Q. Y. Wang, Z. Li, W. H. Zhang, Z. C. Zhang, J. S. Zhang, W. Li, H. Ding, Y. B. Ou, P. Deng, K. Chang, J. Wen, C. L. Song, K. He, J. F. Jin, S. H. Ji, Y. Y. Wang, L. L. Wang, X. Chen, X. C. Ma, Q. K. Xue, *Chin. Phys. Lett.* **2012**, 29, 037402.
- [9] K. Ueda, H. Tabata, T. Kawai, *Science* **1998**, 280, 1064.
- [10] J. A. Mundy, C. M. Brooks, M. E. Holtz, J. A. Moyer, H. Das, A. F. Rébola, J. T. Heron, J. D. Clarkson, S. M. Disseler, Z. Q. Liu, A. Farhan, R. Held, R. Hovden, E. Padgett, Q. Y. Mao, H. Paik, R. Misra, L. F. Kourkoutis, E. Arenholz, A. Scholl, J. A. Borchers, W. D. Ratcliff, R. Ramesh, C. J. Fennie, P. Schiffer, D. A. Muller, D. G. Schlom, *Nature* **2016**, 537, 523.
- [11] M. Gibert, P. Zubko, R. Scherwitzl, J. Íñiguez, J. M. Triscone, *Nat. Mater.* **2012**, 11, 195.
- [12] B. Chen, H. Xu, C. Ma, S. Mattauch, D. Lan, F. Jin, Z. Guo, S. Y. Wan, P. F. Chen, G. Y. Gao, F. Chen, Y. X. Su, W. B. Wu, *Science* **2017**, 357, 191.
- [13] A. K. Yadav, C. T. Nelson, S. L. Hsu, Z. Hong, J. D. Clarkson, C. M. Schlepütz, A. R. Damodaran, P. Shafer, E. Arenholz, L. R. Dedon, D. Chen, A. Vishwanath, A. M. Minor, L. Q. Chen, J. F. Scott, L. W. Martin, R. Ramesh, *Nature* **2016**, 530, 198.
- [14] H. Zheng, J. Wang, S. E. Lofland, Z. Ma, L. Mohaddes-Ardabili, T. Zhao, L. Salamanca-Riba, S. R. Shinde, S. B. Ogale, F. Bai, D. Viehland, Y. Jia, D. G. Schlom, M. Wuttig, A. Roytburd, R. Ramesh, *Science* **2004**, 303, 661.
- [15] A. P. Chen, Q. Su, H. Han, E. Enriquez, Q. X. Jia, *Adv. Mater.* **2019**, 31, 1803241.
- [16] R. J. Zeches, M. D. Rossell, J. X. Zhang, A. J. Hatt, Q. He, C. H. Yang, A. Kumar, C. H. Wang, A. Melville, C. Adamo, G. Sheng, Y.-H. Chu, J. F. Ihlefeld, R. Erni, C. Ederer, V. Gopalan, L. Q. Chen, D. G. Schlom, N. A. Spaldin, L. W. Martin, R. Ramesh, *Science* **2009**, 326, 977.
- [17] J. X. Zhang, B. Xiang, Q. He, J. Seidel, R. J. Zeches, P. Yu, S. Y. Yang, C. H. Wang, Y.-H. Chu, L. W. Martin, A. M. Minor, R. Ramesh, *Nat. Nanotechnol.* **2011**, 6, 98.
- [18] J. Ma, J. Ma, Q. H. Zhang, R.-C. Peng, J. Wang, C. Liu, M. Wang, N. Li, M. F. Chen, X. X. Cheng, P. Gao, L. Gu, L.-Q. Chen, P. Yu, J. X. Zhang, C.-W. Nan, *Nat. Nanotechnol.* **2018**, 13, 947.
- [19] X. Z. Chen, X. D. Fan, L. Li, N. Zhang, Z. J. Niu, T. F. Guo, S. H. Xu, H. Xu, D. L. Wang, H. Y. Zhang, A. S. Mcleod, Z. L. Luo, Q. Y. Lu, A. J. Millis, D. N. Basov, M. K. Liu, C. G. Zeng, *Nat. Phys.* **2020**, 16, 631.
- [20] E.-J. Guo, R. Desautels, D. Keavney, M. A. Roldan, B. J. Kirby, D. Lee, Z. L. Liao, T. Charlton, A. Herklotz, T. Z. Ward, M. R. Fitzsimmons, H. N. Lee, *Sci. Adv.* **2019**, 5, eaav5050.
- [21] H. W. Guo, S. Dong, P. D. Rack, J. D. Budai, C. Beekman, Z. Gai, W. Siemons, C. M. Gonzalez, R. Timilsina, A. T. Wong, A. Herklotz, P. C. Snijders, E. Dagotto, T. Z. Ward, *Phys. Rev. Lett.* **2015**, 114, 256801.
- [22] A. Herklotz, G. Zheng, S. Yogesh, H. Amanda, S. F. Rus, S. Lu, J. Shen, P. D. Rack, *Adv. Sci.* **2018**, 5, 1800356.
- [23] P.-C. Wu, C.-C. Wei, Q. Zhong, S.-Z. Ho, Y.-D. Liou, Y.-C. Liu, C.-C. Chiu, W.-Y. Tzeng, K.-E. Chang, Y.-W. Chang, J. Zheng, C.-F. Chang, C.-M. Tu, T.-M. Chen, C.-W. Luo, R. Huang, C.-G. Duan, Y.-C. Chen, C.-Y. Kuo, J.-C. Yang, *Nat. Commun.* **2022**, 13, 2565.
- [24] D. Lu, D. J. Baek, S. S. Hong, L. F. Kourkoutis, Y. Hikita, H. Y. Hwang, *Nat. Mater.* **2016**, 15, 1255.
- [25] G. H. Dong, S. Z. Li, M. T. Yao, Z. Y. Zhou, Y.-Q. Zhang, X. Han, Z. L. Luo, J. X. Yao, B. Peng, Z. Q. Hu, H. B. Huang, T. T. Jia, J. Y. Li, W. Ren, Z. G. Ye, X. D. Ding, J. Sun, C.-W. Nan, L. Q. Chen, J. Li, M. Liu, *Science* **2019**, 366, 475.
- [26] D. X. Ji, S. H. Cai, T. R. Paudel, H. Y. Sun, C. C. Zhang, L. Han, Y. F. Wei, Y. P. Zang, M. Gu, Y. Zhang, W. P. Gao, H. X. Huyan, W. Guo, D. Wu, Z. Gu, E. Y. Tsymlal, P. Wang, Y. F. Nie, X. Q. Pan, *Nature* **2019**, 570, 87.
- [27] M. Itoh, I. Natori, S. Kubota, M. Kiyochiro, *J. Phys. Soc. Jpn.* **1994**, 63, 1483.
- [28] A. Herklotz, M. D. Biegalski, H. M. Christen, E. J. Guo, K. Nenkov, A. D. Rata, L. Schultz, K. Doerr, *Philos. Trans. R. Soc., A* **2012**, 372, 20120441.
- [29] E. J. Guo, R. Desautels, D. Lee, M. A. Roldan, Z. L. Liao, T. Charlton, H. Ambaye, J. Molaison, R. Boehler, D. Keavney, A. Herklotz, T. Z. Ward, H. N. Lee, M. R. Fitzsimmons, *Phys. Rev. Lett.* **2019**, 122, 187202.
- [30] Y. H. Liu, X. Ke, *J. Phys.: Condens. Matter* **2015**, 27, 373003.
- [31] E. J. Guo, R. D. Desautels, D. Keavney, A. Herklotz, T. Z. Ward, M. R. Fitzsimmons, H. N. Lee, *Phys. Rev. Mater.* **2019**, 3, 014407.
- [32] Z. Li, Y. Wang, G. Tian, P. Li, L. Zhao, F. Zhang, J. Yao, H. Fan, X. Song, D. Chen, Z. Fan, M. Qin, M. Zeng, Z. Zhang, X. Lu, S. Hu, C. Lei, Q. Zhu, J. Li, X. Gao, J.-M. Liu, *Sci. Adv.* **2017**, 3, e1700919.
- [33] P. Zubko, G. Catalan, A. Buckley, P. R. L. Welche, J. F. Scott, *Phys. Rev. Lett.* **2007**, 99, 167601.
- [34] Y. Cao, V. Fatemi, A. Demir, S. Fang, S. L. Tomarken, J. Y. Luo, J. D. Sanchez-Yamagishi, K. Watanabe, T. Taniguchi, E. Kaxiras, R. C. Ashoori, P. Jarillo-Herrero, *Nature* **2018**, 556, 80.
- [35] M. F. Chisholm, W. Luo, M. P. Oxley, S. T. Pantelides, H. N. Lee, *Phys. Rev. Lett.* **2010**, 105, 197602.
- [36] E.-J. Guo, Y. Liu, C. Sohn, R. D. Desautels, A. Herklotz, Z. Liao, J. Nichols, J. W. Freeland, M. R. Fitzsimmons, H. N. Lee, *Adv. Mater.* **2018**, 30, 1705904.